NANO LETTERS

Letter

pubs.acs.org/NanoLett

In Situ Observation of Divergent Phase Transformations in Individual Sulfide Nanocrystals

Matthew T. McDowell,[†] Zhenda Lu,[†] Kristie J. Koski,[‡] Jung Ho Yu,[†] Guangyuan Zheng,[§] and Yi Cui*[,†,∥]

[†]Department of Materials Science and Engineering, Stanford University, Stanford, California 94305, United States

[‡]Department of Chemistry, Brown University, Providence, Rhode Island 02912, United States

[§]Department of Chemical Engineering, Stanford University, Stanford, California 94305, United States

[∥]Stanford Institute for Materials and Energy Sciences, SLAC National Accelerator Laboratory, 2575 Sand Hill Road, Menlo Park, California 94025, United States

Supporting Information

ABSTRACT: Inorganic nanocrystals have attracted widespread attention both for their size-dependent properties and for their potential use as building blocks in an array of applications. A complete understanding of chemical transformations in nanocrystals is important for controlling structure, composition, and electronic properties. Here, we utilize in situ high-resolution transmission electron microscopy to study structural and morphological transformations in individual sulfide nanocrystals (copper sulfide, iron sulfide, and cobalt sulfide) as they react with lithium. The experiments reveal the influence of structure and composition on the transformation pathway (conversion versus displacement reactions), and they provide a high-resolution view of the unique displacement reaction mechanism in copper sulfide in which copper metal is extruded from the crystal. The structural similarity between the initial and final phases, as well as the mobility of ions within the crystal, are seen to exert a controlling influence on the reaction pathway.

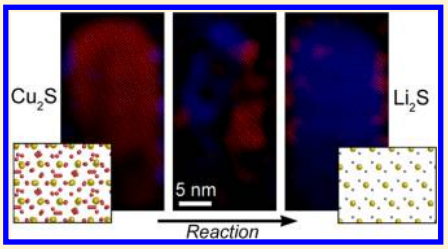

KEYWORDS: *Chalcogenide nanocrystals, phase transformations, conversion reactions, displacement reactions, in situ TEM*

The synthesis of inorganic nanocrystals with tailored shape, size, composition, structure, and physicochemical properties is a major focus in the field of nanoscience.[1,2] Controlled nanocrystal synthesis has been motivated both by a desire to understand the unique size-dependent properties of nanocrystals[3] as well as by their potential for use as building blocks in applications such as solar cells,[4] thermoelectrics,[5] batteries,[6] and optical devices.[7] For full control of nanoscale chemistry and for use in applications, it is important to develop an atomic scale understanding of nanocrystal synthesis, phase transformations, and chemical reactions. Because of the small size of nanocrystals, in situ transmission electron microscopy (TEM) has proven to be useful in characterizing such dynamic processes in these structures[8−12] but much remains to be understood.

Chemical transformations are an important aspect of nanocrystal synthesis and processing; in many cases, as-synthesized nanocrystals are made to undergo further chemical transformation either during the fabrication of more complex structures[13,14] or in the operation of a device, such as a battery electrode.[6] As such, it is necessary to understand structural dynamics and transformation pathways during the chemical or electrochemical reaction of individual nanocrystals with a separate species. Recently, in situ TEM techniques for monitoring the electrochemical reaction of nanostructures with another elemental species, such as lithium or sodium, have been developed.[15] This type of experiment has been exceedingly useful for exploring the nanoscale reaction mechanisms in a variety of novel lithium battery electrode materials, such as silicon and germanium.[16−23] In addition, a number of recent studies have explored nanocrystal reactions;[24−26] in one, the reaction of lithium with groups of FeF_2 nanoparticles was examined, revealing structural evolution during the conversion reaction of FeF_2 to form amorphous LiF and Fe nanodomains.[24] Many oxide and sulfide nanomaterials react with lithium through such conversion reactions but the effect of structure and composition on reaction pathway has not been fully investigated. Here, we utilize an experimental framework suitable for the high-resolution TEM observation of chemical transformations in individual sulfide nanocrystals as they react with lithium, and we explore both the atomic-level dynamics and the divergent reaction pathways (displacement versus conversion reactions) in crystals with different chemistry and structure.

These experiments utilize a sample holder that allows for the creation of a nanoscale electrochemical cell within the TEM.[15,17] As shown in Figure 1a, the holder features two metallic probes that can be moved via piezo control. On the left probe, a piece of lithium metal coated with a thin (~100 nm) layer of lithium oxide/nitride acts as the lithium source.

Received: November 18, 2014
Revised: January 5, 2015

DOI: 10.1021/nl504436m
Nano Lett. XXXX, XXX, XXX−XXX

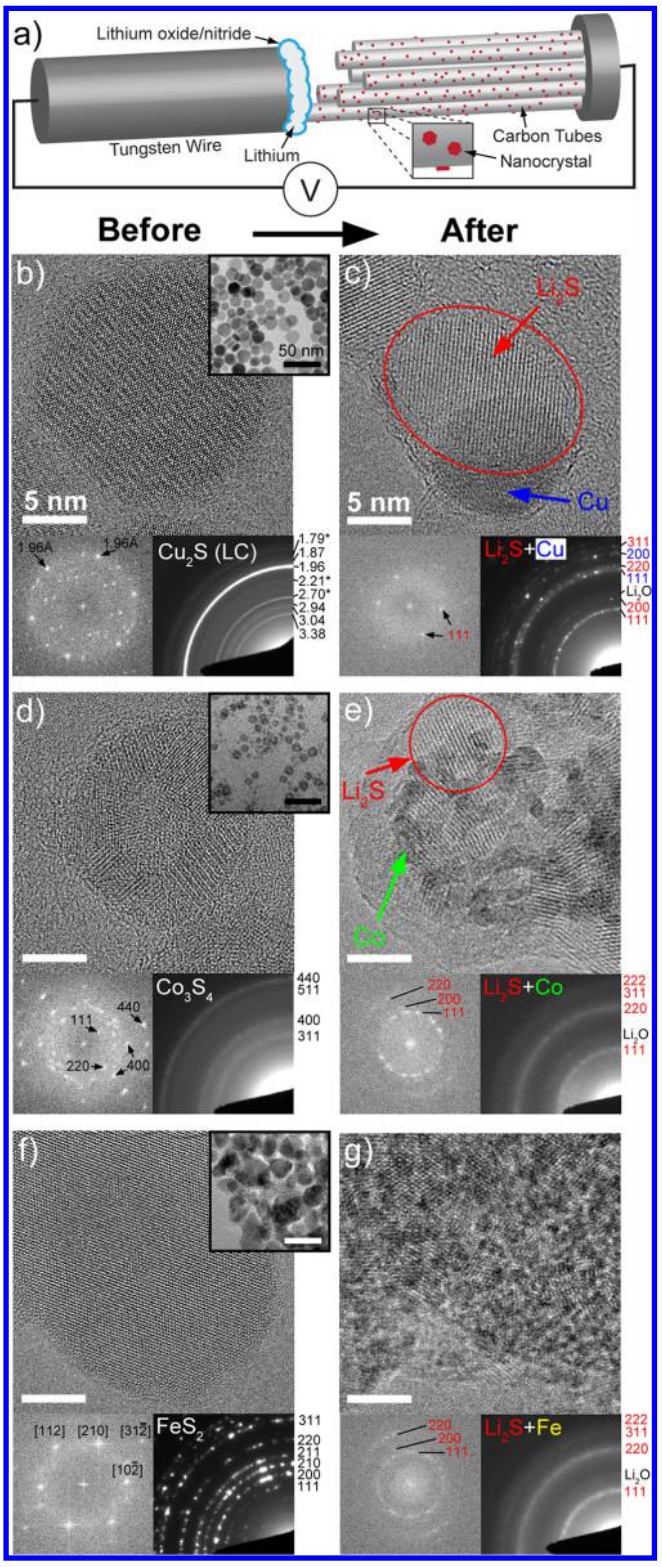

Figure 1. Reaction of different sulfide nanocrystals with lithium. (a) Schematic of in situ TEM setup showing nanocrystals supported on carbon tubes. (b–g) TEM characterization of three different types of nanocrystals before and after reaction with lithium. (b) Image of a single Cu_2S nanocrystal along with the associated fast Fourier transform (FFT), low-magnification view of a collection of particles, and SAED pattern of multiple particles showing the low chalcocite phase. The SAED pattern is labeled with planar spacings (in Å); diffraction rings distinguishing the LC phase are noted with asterisks. (c) TEM characterization of a similar nanocrystal after reaction with lithium. Single Li_2S and copper metal domains are visible; the corresponding FFT indicates that the image shows {111} Li_2S planes. The SAED pattern (from a lower-magnification view of many crystals) shows characteristic diffraction from Li_2S, copper, and Li_2O (which forms due to reaction of lithium with surface oxygen on the carbon support). The rings are labeled with color-coded Miller indices (red for Li_2S, blue for copper, and black for Li_2O {111}). (d) TEM characterization of a hollow polycrystalline Co_3S_4 nanocrystal with the spinel structure. (e) A similar Co_3S_4 nanocrystal after reaction with lithium showing a polycrystalline mixture of many Li_2S and cobalt metal domains. Darker cobalt nanoparticles are visible, as well as lighter lattice fringes that correspond to Li_2S crystals (as evidenced in the FFT). The SAED pattern reveals diffraction rings from Li_2S but cobalt diffraction rings are not discernible due to the very small size of the cobalt nanoparticles, which leads to broad and weak diffraction rings. (f) TEM characterization of a pyrite FeS_2 nanocrystal. (g) A single FeS_2 nanocrystal after reaction with lithium showing a polycrystalline mixture of Li_2S and Fe metal similar to the Co_3S_4 case. Again, the Fe diffraction rings are not easily discernible in the SAED pattern because of the small crystallite size; in addition, the Fe rings overlap with the Li_2S rings.

Attached to the right probe is a collection of carbon tubes ~300 nm in diameter with ~20 nm wall thickness onto which nanocrystals are deposited. Inside the microscope, the lithium metal electrode is positioned so that it is touching a carbon tube. The oxide/nitride layer on the surface of the lithium metal prevents direct chemical reaction and acts as a solid electrolyte layer through which lithium ions can flow.[16] By negatively biasing the carbon electrode versus the lithium electrode (usually to −2.5 V), Li^+ ions flow through the solid electrolyte and are reduced at the carbon electrode, where lithium then diffuses through and on the surface of the carbon to react with the attached nanocrystals. In this way, the carbon tubes provide both a path for lithium transport and a stable support allowing for high-resolution TEM (HRTEM) imaging of the reaction process in the nanocrystals. It should be emphasized that the Li^+ ions are reduced at the carbon electrode before they diffuse to the nanocrystals, meaning that chemical reactions with lithium (instead of electrochemical reactions) are observed in the nanocrystals.

Figure 1b,d,f shows example TEM images of the three different types of sulfide nanocrystals considered in this study (synthesis methods are presented in the Supporting Information). Cu_2S nanocrystals (Figure 1b) are shaped as hexagonal disks ~15–18 nm wide and ~5–8 nm thick.[27] The hexagonal shape arises because the crystal structure consists of a slightly distorted hexagonal close-packed (hcp) sulfur sublattice with the *c*-axis perpendicular to the disk face; copper is distributed both within and between the close-packed sulfur layers. The $Cu_{2-x}S$ system exhibits rich crystal chemistry with a variety of closely related phases that exist.[28,29] Stoichiometric Cu_2S can exist either as the low chalcocite (LC) or high chalcocite (HC) phase, both of which feature the hcp sulfur sublattice with different copper arrangements. In the HC phase (stable above 103.5 °C in the bulk), the copper atoms are highly disordered, and the crystallography of the structure is defined by the hexagonal sulfur framework (space group $P6_3/mmc$).[28,29] In the LC phase, which is stable below this transition temperature, the copper atoms are fixed in a complex interstitial manner, giving rise to monoclinic symmetry (space group $P2_1/c$).[28,30] In addition, another stable low-temperature phase exists, djurleite

DOI: 10.1021/nl504436m
Nano Lett. XXXX, XXX, XXX–XXX

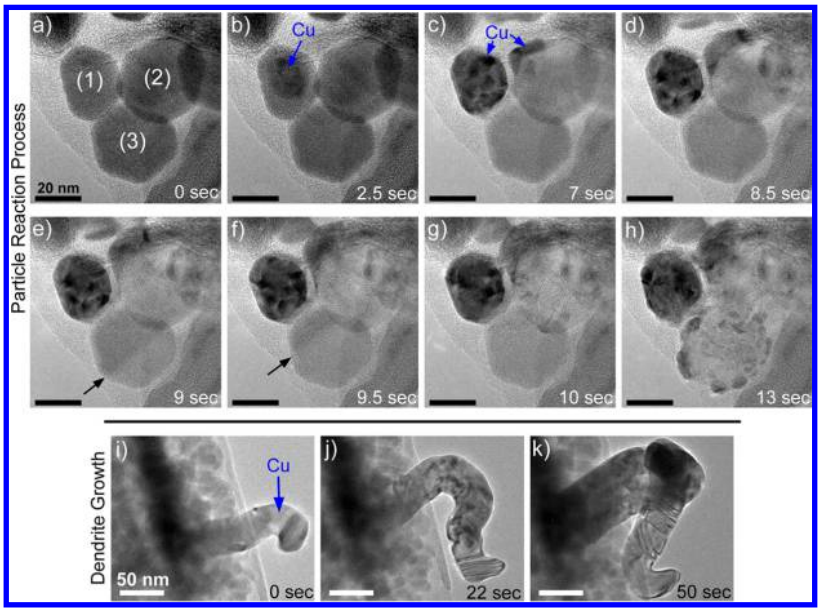

Figure 2. Reaction of groups of Cu_2S nanocrystals. (a–h) Time-series of a reaction of a group of larger Cu_2S nanocrystals. (a) Top-down view of three Cu_2S crystals that are initially in contact. (b) The reaction with lithium begins, and copper metal begins to form on the surface of particle 1 as copper is removed from this particle. (c,d) The copper metal domain on particle 1 grows larger, and copper is also removed from particle 2 to form a domain on the edge of this particle. (e–g) A reaction front (marked by arrows) sweeps across particle 3 as copper is partially removed from this particle to join with the already-formed copper metal domains on the other particles. (h) The remaining copper is ejected from particle 3 to form a multitude of copper metal domains on the surface of the particle. All the original Cu_2S particles have been transformed to Li_2S with copper domains residing on the surface of the new particles. (i–k) Time series of a different group of particles showing the formation of a copper dendrite when a larger group of Cu_2S particles reacts with lithium. The darker region to the left in the images is a thick group of Cu_2S particles supported by carbon. The copper ions are mobile enough to diffuse from particle to particle during the reaction, resulting in the growth of a copper dendrite during the formation of Li_2S.

($Cu_{1.93-1.97}S$). The structure of djurleite is similar to LC, as it also features the hcp sulfur sublattice with different copper ordering (space group $P2_1/n$).[28,31] LC and djurleite are often found intermixed[28] and there is actually a thermodynamic tendency for copper deficiency (djurleite formation) in this system.[32,33] LC can transform to djurleite through copper vacancy formation due to oxidation or other processes.[33,34] Nanocrystals of all three phases have been reported[27,35] but due to similar diffraction patterns and variable diffraction peak intensity for nanocrystals it is often difficult to discern between the LC and djurleite phases.[33,35,36] In the present study, based on selected area electron diffraction (SAED, Figure 1b), the as-synthesized nanocrystals appear to have the LC phase due to the often-observed presence of certain characteristic diffraction spots/rings (see Supporting Information for details). However, we do not rule out the presence of djurleite due to varying intensity of the characteristic LC rings. As such, we conclude that we have primarily LC crystals with the possible inclusion of some djurleite crystals. The situation is further complicated by the fact that LC nanocrystals have been shown to transform to the HC phase due to beam-induced heating during HRTEM imaging.[8] Despite this complex phase space, it will be demonstrated that for our experiments the precise arrangement of copper is not as important as the structure of the sulfur sublattice, which is very similar for all the phases. With this understanding, we use the terminology "Cu_2S" to refer to these crystals.

The other two nanocrystals studied here are Co_3S_4 (Figure 1d) and FeS_2 (Figure 1f). The Co_3S_4 nanocrystals (cubic spinel, space group $Fd\bar{3}m$) are polycrystalline hollow spheres between 10 and 15 nm in diameter.[37] The FeS_2 crystals are single crystalline with the pyrite structure (cubic, space group $Pa\bar{3}$)[38] and they have a broader size range than either the Co_3S_4 or the Cu_2S. Schematics of the structures of these two materials are presented in the Supporting Information.

The three types of nanocrystals have different compositions, morphologies, crystal structures, and transition metal oxidation states. However, these three phases should undergo the same thermodynamically favorable reaction with lithium at the applied potential in these experiments

$$2y\mathrm{Li}^+ + \mathrm{M}_x\mathrm{S}_y + 2y\mathrm{e}^- \rightarrow y\mathrm{Li}_2\mathrm{S} + x\mathrm{M} \quad (1)$$

where M is the transition metal species. Figure 1c,e,g shows each type of nanocrystal after reaction with lithium. Both Co_3S_4 and FeS_2 crystals transform into a polycrystalline mixture of Li_2S and finely dispersed metallic cobalt or iron (Figure 1e,g). Li_2S takes the cubic antifluorite structure (space group $Fm\bar{3}m$) with the sulfur located on a face-centered cubic (fcc) sublattice and the lithium filling all the tetrahedral interstices. The lighter lattice fringes in the images correspond to Li_2S planes, while the darker areas are the metallic nanodomains. This type of intimately mixed morphology is characteristic of a conversion reaction in which the initial crystal decomposes to form interspersed Li_2S and metallic domains; conversion reactions have been widely reported for a variety of materials during reaction with lithium, including oxides, sulfides, and fluorides.[6,24,39,40] Other in situ TEM studies have also shown similar conversion reactions when CoS_2 and Co_9S_8 react with lithium.[41,42] Corresponding videos of the reaction of Co_3S_4 and FeS_2 particles are available in the Supporting Information. The lithiation of FeS_2 particles proceeds via the radial movement of a reaction front into the particle, which consumes the FeS_2 and leaves behind intermixed Li_2S and Fe nanodomains with a

DOI: 10.1021/nl504436m
Nano Lett. XXXX, XXX, XXX–XXX

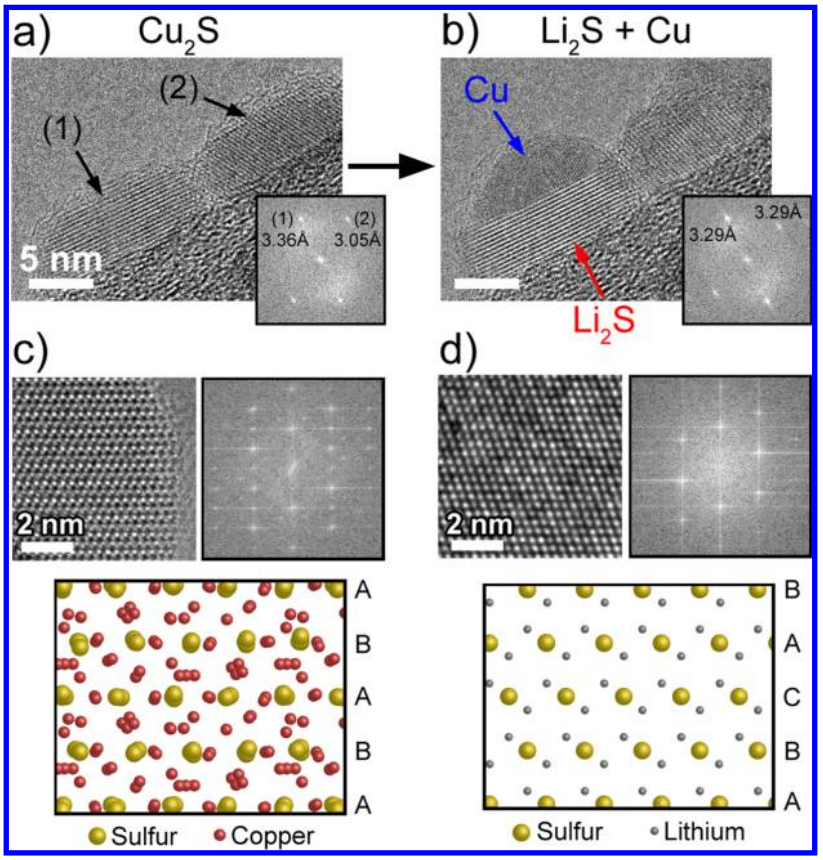

Figure 3. Transformation of the Cu_2S crystal structure during the reaction. (a) Edge-on view of two small Cu_2S nanocrystals (labeled 1 and 2) supported on the outer wall of a carbon tube. The (002) planes of the hexagonal sulfur sublattice (with spacing of ~3.36 Å, as shown in the FFT) are visible in particle 1, while (101) planes of the hexagonal sulfur sublattice (with spacing of ~3.05 Å) are visible in particle 2. (b) The same two particles after reaction with lithium 0.5 s later. Both particles have transformed to Li_2S while maintaining their original shape, and the extruded copper metal has formed a cap on top of particle 1. The transformation of particle 1 occurs through a slight decrease (~2%) in the spacing of the close-packed planes of the sulfur sublattice (i.e., the (002) planes of the hexagonal sublattice of Cu_2S) to match the $Li_2S(111)$ planar spacing of 3.29 Å, as shown in the FFT. In particle 2, the original planes rotate slightly as new $Li_2S(11\bar{1})$ planes become visible. (c) High-resolution image of a different Cu_2S particle along the [010] zone axis of the hexagonal sulfur sublattice. Note that the FFT indicates that this particle exhibits characteristics of high chalcocite,[8] which could be caused by beam-induced heating. The ABAB stacking of the sulfur sublattice is apparent, as shown in the accompanying schematic of low chalcocite below the TEM image.[8,28] The image was taken at 300 kV with an aberration-corrected instrument. (d) High-resolution image of a reacted Li_2S particle along the $[\bar{1}10]$ zone axis of Li_2S. The ABC stacking is apparent, as shown in the accompanying schematic below the image. The image was taken at 200 kV without aberration correction. Overall, the arrangement of the sulfur sublattice in the two phases is very similar; the particles can transform via a shift from ABAB stacking to ABC stacking of the sublattice in conjunction with a slight decrease in the spacing of the close-packed planes.

larger total volume. In Supporting Information video S5, this reaction front is evident between the inner FeS_2 region with darker contrast and the exterior reacted region, which has lighter contrast. The much smaller Co_3S_4 particles appear to transform uniformly into a mixture of Li_2S and Co (Supporting Information video S4), although this is probably because a reaction front moved too quickly to detect with the video recording frame rate utilized (2 frames per second). In contrast to this final mixed morphology, each Cu_2S crystal usually reacts with lithium to form distinct domains of crystalline Li_2S and copper metal, where the copper domain forms at the surface of a single converted Li_2S particle (Figure 1c). The details of and reasons for this divergent reaction behavior will be the primary focus of the reminder of the paper. Note that the Supporting Information contains further characterization of these reaction products, including energy dispersive spectroscopy (EDS) and electron energy loss spectroscopy (EELS) data. In addition, control experiments revealed that electron beam exposure did not alter the morphology of the pristine nanoparticles and examination of reacted material both under continuous beam exposure as well as material that underwent reaction away from the beam showed no differences in product morphology or structure (this is demonstrated in the Supporting Information). Thus, it was concluded that electron beam effects did not significantly affect the experiments.

To study detailed reaction mechanisms and to explore the effect of size, larger Cu_2S nanocrystals were synthesized via a slightly different method (see Supporting Information for details) and observed during reaction with lithium. These crystals are typically about 30−40 nm wide and 15 nm thick. Figure 2 shows the reaction process in three crystals that are in physical contact with each other; Figure 2a is an image immediately before reaction with lithium. In Figure 2b, the reaction process has started, and copper is being ejected and is accumulating as copper metal on the surface of particle 1. In Figure 2c,d, the copper domain on the surface of particle 1 grows larger, and a new copper metal domain forms at the edge of particle 2 as copper is removed from this particle. Figure 2e−g reveals the movement of a reaction front across particle 3 as copper is partially removed from this particle. Interestingly, the

DOI: 10.1021/nl504436m
Nano Lett. XXXX, XXX, XXX−XXX

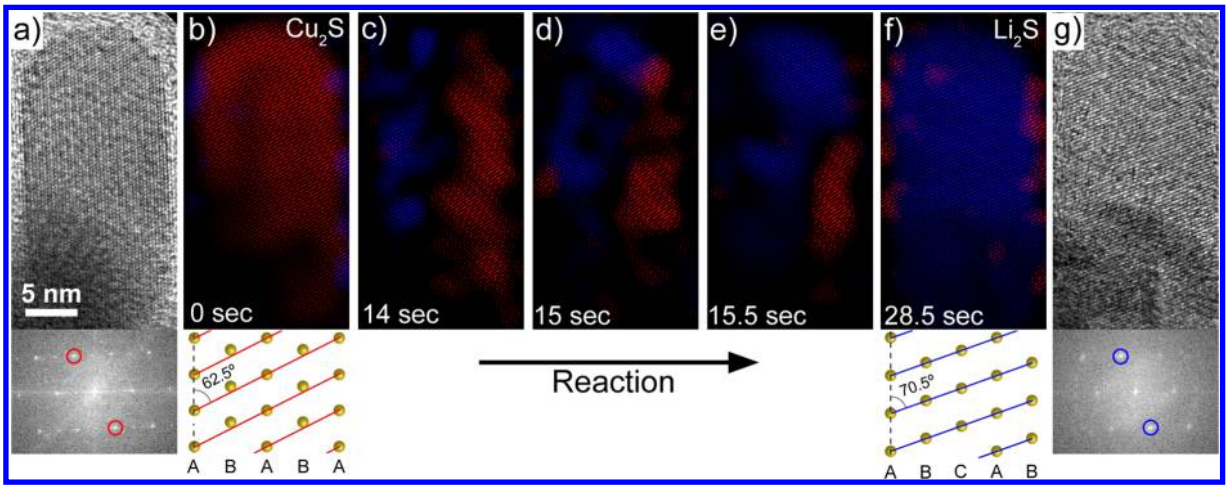

Figure 4. Observation of the reaction pathway in a single Cu_2S nanocrystal. (a) Edge-on view of a Cu_2S nanocrystal disk 29 nm wide and 14 nm thick. The FFT shows that this is again a view along the [010] zone axis of the hexagonal sulfur sublattice. (b) Fourier-filtered image of the nanocrystal with (101) planes displayed in red (the spots corresponding to these planes are circled in the FFT in (a)). The schematic of the sulfur sublattice in (b) shows these planes as red lines. The planes are ~62.5° from the vertical close-packed sulfur layers; this angle and the planar spacing are characteristic of the ABAB stacking sequence of the Cu_2S structure. (c–f) Fourier-filtered images during reaction with lithium showing the disappearance of the Cu_2S region and the emergence of a new set of planes in blue. As shown in the schematic in (f), these are the $(11\bar{1})$ planes of the Li_2S structure viewed along the $[\bar{1}10]$ zone axis, which have a larger planar spacing and are oriented at ~70.5° from the (111) planes stacked parallel to the disk face. The images in (c–f) show that the transformed Li_2S region sweeps across the crystal from the left to the right over the course of a few seconds, and at intermediate times both structures exist in the particle. Note that there is a slight contraction in the (002) close-packed planar spacing of the Cu_2S hexagonal sulfur sublattice before this transformation takes place (not shown here); this could be due to the initial partial removal of some of copper and replacement with lithium. (g) TEM image and FFT after the reaction; the crystal has transformed to the Li_2S phase while maintaining the original shape.

ejected copper metal is not deposited on the surface of particle 3, but instead it appears that the copper ions diffuse from particle 3 through the other particles to join with the already-formed copper metal domains. In Figure 2h, the reaction is complete, and the remaining copper has been ejected from particle 3 to form small copper domains attached to the surface of the newly formed Li_2S particle. The two-step reaction process seen in particle 3 was commonly (although not always) observed in these larger crystals: first, some copper is removed via the sweep of a reaction front across the particle, and then the remaining copper is ejected to form smaller domains. In other cases, a distinct reaction front was not observed while copper formed at the surface, but this may be because the particle was not oriented favorably for viewing the reaction front motion. In addition, sometimes the reaction was observed to occur only via the movement of a reaction front without the second ejection step. Video S1 in the Supporting Information shows the dynamic reaction process of these particles.

The transport of copper ions through or on the surface of neighboring Cu_2S particles during reaction was also observed on a larger scale than just a few particles, leading to the dramatic growth of dendrites from large agglomerations of Cu_2S particles (Figure 2i–k). In these images, a copper metal dendrite is growing into the vacuum of the TEM column from the edge of a group of Cu_2S particles that are reacting with lithium. Dendrites often formed when many particles were in contact and when the reaction process was relatively slow. Assuming the rate of copper transport is fast enough, the formation of large copper dendrites may be driven by the energetic benefit of a smaller surface area to volume ratio for the newly formed copper metal.

Overall, it is clear that the extrusion process observed for the Cu_2S reaction is different than the previously discussed conversion reaction in Co_3S_4 and FeS_2, which results in nanometer-scale clusters of metal mixed with Li_2S. The reaction of Cu_2S is more akin to a displacement reaction, which has previously been observed in conventional electrochemical experiments with other copper-containing materials such as $Cu_{2.33}V_4O_{11}$, $Cu_3Mo_6S_8$, CuS, and a few others.[40,43,44] Interestingly, in the case of $Cu_{2.33}V_4O_{11}$ the displacement reaction was observed to be electrochemically reversible, and scanning electron microscopy showed the reincorporation of copper dendrites during lithium removal.[43] In addition, it has been reported that copper sulfides exhibit lower charge/discharge overpotentials relative to other materials that undergo conversion reactions, suggesting more facile kinetics during the reaction.[45] The unique extrusion mechanism is thought to arise when two conditions are met: (i) the initial phase must exhibit high ionic conductivity to allow for fast transport of the transition metal ion, and (ii) there must be a structural relationship between the initial and final phases to allow for a kinetically facile transformation to the new phase.[40] The various $Cu_{2-x}S$ phases are known for their high ionic diffusivity of copper; in particular, the HC phase has extremely high fluidlike ion mobility owing to the disordered distribution of copper and the large number of copper vacancies.[28,46] The chemical diffusion coefficient of Cu in HC Cu_2S has been found to be 2×10^{-7} $cm^2 \cdot s^{-1}$.[47] The LC and djurleite phases exhibit lower copper ion diffusion coefficients ($\tilde{D}_{Cu} = \sim 10^{-7}$–$10^{-8}$ $cm^2 \cdot s^{-1}$ for LC at room temperature; $\tilde{D}_{Cu} = \sim 10^{-9}$ $cm^2 \cdot s^{-1}$ for djurleite at room temperature)[48] but the diffusivities are still much higher than other metal sulfides such as FeS_2 ($\tilde{D}_{Fe} = \sim 10^{-17}$ $cm^2 \cdot s^{-1}$ in FeS_2 at 100 °C).[49] Regarding the structural requirement for the displacement reaction, there are significant crystallographic similarities between Cu_2S and Li_2S,[40] which will be discussed at length in the following section. The other two sulfide phases studied here do not meet these requirements, which is why the reaction product morphology is

DOI: 10.1021/nl504436m
Nano Lett. XXXX, XXX, XXX–XXX

consistent with the more common conversion reaction mechanism. In addition, another difference is that the transition metals in FeS_2 and Co_3S_4 have higher oxidation states than copper in Cu_2S, meaning that more lithium atoms are required per transition metal for the complete reaction.

Further high-resolution study of this reaction allows for the determination of structural and morphological relationships between the initial and final crystals. Figure 3a shows an edge-on view of two smaller Cu_2S nanocrystals supported on the sidewall of a carbon tube. In particle 1, the (002) planes of the hcp sulfur sublattice are visible. Note that for clarity, we will use the Miller indices of the hexagonal sulfur sublattice instead of the indices of the much larger monoclinic unit cell. After reaction (only ~0.5 s later), copper has been extruded from the particles, and a hemispherical copper metal cap is visible on top of particle 1. The original Cu_2S particles have been transformed into Li_2S particles with the morphology of the two particles remaining largely unchanged. In fact, here we only observe a ~2% contraction in the close-packed planar spacing and a slight change in contrast that signifies the transformation of particle 1 from Cu_2S to Li_2S. The transformation of the individual particles from the Cu_2S structure to the Li_2S structure with negligible change in particle morphology is enabled by the structural similarities between the two phases, as shown by schematics and HR zone axis images of different particles in Figure 3c,d. The key to the transformation is that the sulfur sublattice only slightly shifts; the spacing of the close-packed sulfur planes is similar, but the sulfur sublattice stacking sequence changes from ABAB in the Cu_2S phase to ABCABC in the cubic Li_2S phase (see schematics in Figure 3c,d). This is in contrast with the FeS_2 and Co_3S_4 phases, which exhibit more significant structural differences compared to Li_2S (see the Supporting Information for structural schematics of these materials). The pyrite FeS_2 structure features pairs of sulfur atoms distributed within an fcc iron sublattice, and these pairs must be rearranged during reaction. The Co_3S_4 spinel structure features an fcc sulfur sublattice with cobalt arranged on tetrahedral and octahedral interstitial positions, but the {111} planar spacing is 20% smaller than Li_2S, which necessitates significant volume changes during the reaction of this material.

Some parallels can be drawn between the reaction of Cu_2S studied here and solution phase cation exchange reactions, such as ion exchange to form Ag_2Se from CdSe nanocrystals. A cation exchange reaction involves complete replacement of the cations without change of the oxidation state and with only minor structural changes in the anion sublattice.[13] The ion exchange reaction, however, is a double replacement reaction, whereas the reaction of lithium with Cu_2S in this study is an electrochemical redox reaction. Despite the differences in chemistry, the structural rearrangement of the anion sublattice could be similar in both cases.

The question now arises as to the pathway of the sublattice shift from ABAB to ABC stacking. In Figure 4, the transformation is visualized in a single nanocrystal. Figure 4a shows a TEM image of the unreacted crystal; this is an edge-on view along the [010] zone axis of the hexagonal sulfur sublattice. Figure 4b–f shows colored Fourier-filtered images of this crystal at different times during the reaction showing the location of two different sets of planes: the (101) planes of the hexagonal sulfur sublattice in Cu_2S (subsequently denoted "hcp stacking") and a related set of $(11\bar{1})$ planes of the Li_2S lattice (subsequently denoted "fcc stacking"). These planes are at slightly different angles with respect to the close-packed sulfur layers (as shown in the crystal schematics in Figure 4b,f), and mapping the location of each set of planes allows for visualization of the extent of the transformed region in this crystal as the reaction progresses. In Figure 4b, hcp stacking (shown in red) is initially present throughout the crystal (i.e., the crystal is Cu_2S). In Figure 4c, the transformation begins on the left side of the crystal with a shift to fcc stacking (shown in blue), and over the next few seconds the transformed region sweeps across the crystal to the right. After reaction, the crystal has transformed to the Li_2S phase while retaining the same morphology (Figure 4f,g). Note that copper metal domains do not form on the surface of this particular crystal; instead, the copper ions removed from this crystal diffuse through other crystals outside of the image frame. The transformed fcc stacking region that appears behind the sweeping reaction front also has lighter contrast in the original TEM images (see Supporting Information), suggesting the full removal of copper and the formation of the Li_2S phase. These data show that the sulfur sublattice undergoes a local shift from hcp to fcc stacking as the lithium enters the structure and the copper is removed with the transformation sweeping across the crystal. This is in contrast to a hypothetical alternative situation in which the entire crystal might undergo a coordinated shear from hcp to fcc stacking; this is not the case, as it seems that the local interaction of the lithium and copper with the sulfur sublattice drives the transformation. Overall, these images reveal important structural details about this transformation and offer a high-resolution glimpse into the dynamics of this reaction in individual nanocrystals.

In conclusion, these experiments have provided an atomic-level view of chemical transformations in different nanocrystals. The transformation pathway during the reaction of Cu_2S crystals with lithium is quite different than that during the reaction of Co_3S_4 or FeS_2. For Cu_2S, copper metal is extruded out of the crystal during the formation of a single Li_2S domain, while for Co_3S_4 and FeS_2 the reaction with lithium results in a nanoscale mixture of Li_2S and cobalt or iron nanoparticles. The displacement reaction in Cu_2S is enabled by the high ionic mobility of copper ions in the structure as well as the similarity of the sulfur sublattices in the initial and final phases. High-resolution imaging revealed that the sulfur sublattice rearranges as copper leaves the structure with close-packed sulfur planes shifting from the hcp-type stacking of Cu_2S to the fcc-type stacking of Li_2S. After reaction, the new Li_2S particle retains the original shape and morphology of the original Cu_2S particle, and the extruded copper either forms particles at the surface or larger dendrites if many Cu_2S crystals are in contact. These experiments show the value of in situ TEM techniques for elucidating complex reaction mechanisms in individual nanocrystals. Further in situ TEM studies on the potential reversibility of this reaction are important to determine if this material is appropriate for use in secondary lithium-ion batteries; therefore, a next step is to study the phase transformations during the delithiation of these various nanocrystals. In addition, due to the formation of Li_2S upon lithiation, metal sulfide-based electrodes are expected to share some similarities with sulfur electrodes for lithium–sulfur batteries. Thus, strategies to minimize the loss of active material due to the dissolution of polysulfides into the electrolyte will be necessary for stable cycling performance in battery cells.[45]

DOI: 10.1021/nl504436m
Nano Lett. XXXX, XXX, XXX–XXX

■ ASSOCIATED CONTENT

Supporting Information

In situ TEM videos of reaction processes, detailed synthetic procedures for nanocrystals, TEM methods, characterization of Cu_2S nanocrystals, structural schematics, and EELS and EDS characterization of reaction products. This material is available free of charge via the Internet at http://pubs.acs.org.

■ AUTHOR INFORMATION

Corresponding Author

*E-mail: yicui@stanford.edu. Phone: 650-723-4613. Fax: 650-725-4034.

Present Address

(M.T.M.) Postdoctoral Scholar, California Institute of Technology, Division of Chemistry and Chemical Engineering.

Author Contributions

M.T.M. conceived the experiments, synthesized and fabricated materials, carried out the experiments and data analysis, and wrote the manuscript. Z.L., K.J.K., J.H.Y., and G.Y. synthesized materials and helped revise the paper. Y.C. cowrote the manuscript and provided guidance.

Notes

The authors declare no competing financial interest.

■ ACKNOWLEDGMENTS

M.T.M. acknowledges support from the National Science Foundation Graduate Fellowship and a Chevron Stanford Graduate Fellowship. This work is supported by the U.S. Department of Energy, Office of Basic Energy Sciences, Division of Materials Sciences and Engineering under Contract No. DE-AC02-76SF00515 through the SLAC National Accelerator Laboratory LDRD project and the Assistant Secretary for Energy Efficiency and Renewable Energy, Office of Vehicle Technologies of the U.S. Department of Energy under Contract No. DE-AC02-05CH11231, Subcontract No. 6951379 under the BATT Program.

■ REFERENCES

(1) Alivisatos, A. P. *Science* **1996**, *271* (5251), 933−937.
(2) Murray, C. B.; Norris, D. J.; Bawendi, M. G. *J. Am. Chem. Soc.* **1993**, *115* (19), 8706−8715.
(3) Chen, C.-C.; Herhold, A. B.; Johnson, C. S.; Alivisatos, A. P. *Science* **1997**, *276* (5311), 398−401.
(4) Tang, J.; Kemp, K. W.; Hoogland, S.; Jeong, K. S.; Liu, H.; Levina, L.; Furukawa, M.; Wang, X.; Debnath, R.; Cha, D.; Chou, K. W.; Fischer, A.; Amassian, A.; Asbury, J. B.; Sargent, E. H. *Nat. Mater.* **2011**, *10* (10), 765−771.
(5) Harman, T. C.; Taylor, P. J.; Walsh, M. P.; LaForge, B. E. *Science* **2002**, *297* (5590), 2229−2232.
(6) Poizot, P.; Laruelle, S.; Grugeon, S.; Dupont, L.; Tarascon, J. M. *Nature* **2000**, *407* (6803), 496−499.
(7) Klimov, V. I.; Ivanov, S. A.; Nanda, J.; Achermann, M.; Bezel, I.; McGuire, J. A.; Piryatinski, A. *Nature* **2007**, *447* (7143), 441−446.
(8) Zheng, H.; Rivest, J. B.; Miller, T. A.; Sadtler, B.; Lindenberg, A.; Toney, M. F.; Wang, L.-W.; Kisielowski, C.; Alivisatos, A. P. *Science* **2011**, *333* (6039), 206−209.
(9) Holmberg, V. C.; Panthani, M. G.; Korgel, B. A. *Science* **2009**, *326* (5951), 405−407.
(10) Zheng, H.; Smith, R. K.; Jun, Y.-w.; Kisielowski, C.; Dahmen, U.; Alivisatos, A. P. *Science* **2009**, *324* (5932), 1309−1312.
(11) Yuk, J. M.; Park, J.; Ercius, P.; Kim, K.; Hellebusch, D. J.; Crommie, M. F.; Lee, J. Y.; Zettl, A.; Alivisatos, A. P. *Science* **2012**, *336* (6077), 61−64.
(12) Yalcin, A. O.; Fan, Z.; Goris, B.; Li, W.-F.; Koster, R. S.; Fang, C.-M.; van Blaaderen, A.; Casavola, M.; Tichelaar, F. D.; Bals, S.; Van Tendeloo, G.; Vlugt, T. J. H.; Vanmaekelbergh, D.; Zandbergen, H. W.; van Huis, M. A. *Nano Lett.* **2014**, *14* (6), 3661−3667.
(13) Son, D. H.; Hughes, S. M.; Yin, Y. D.; Alivisatos, A. P. *Science* **2004**, *306* (5698), 1009−1012.
(14) Ha, D.-H.; Caldwell, A. H.; Ward, M. J.; Honrao, S.; Mathew, K.; Hovden, R.; Koker, M. K. A.; Muller, D. A.; Hennig, R. G.; Robinson, R. D. *Nano Lett.* **2014**, *14* (12), 7090−7099.
(15) Huang, J. Y.; Zhong, L.; Wang, C. M.; Sullivan, J. P.; Xu, W.; Zhang, L. Q.; Mao, S. X.; Hudak, N. S.; Liu, X. H.; Subramanian, A.; Fan, H. Y.; Qi, L. A.; Kushima, A.; Li, J. *Science* **2010**, *330* (6010), 1515−1520.
(16) Liu, X. H.; Zheng, H.; Zhong, L.; Huan, S.; Karki, K.; Zhang, L. Q.; Liu, Y.; Kushima, A.; Liang, W. T.; Wang, J. W.; Cho, J. H.; Epstein, E.; Dayeh, S. A.; Picraux, S. T.; Zhu, T.; Li, J.; Sullivan, J. P.; Cumings, J.; Wang, C. S.; Mao, S. X.; Ye, Z. Z.; Zhang, S. L.; Huang, J. Y. *Nano Lett.* **2011**, *11* (8), 3312−3318.
(17) McDowell, M. T.; Lee, S. W.; Harris, J. T.; Korgel, B. A.; Wang, C. M.; Nix, W. D.; Cui, Y. *Nano Lett.* **2013**, *13* (2), 758−764.
(18) McDowell, M. T.; Ryu, I.; Lee, S. W.; Wang, C. M.; Nix, W. D.; Cui, Y. *Adv. Mater.* **2012**, *24* (45), 6034−6041.
(19) Liang, W.; Yang, H.; Fan, F.; Liu, Y.; Liu, X.-H.; Huang, J. Y.; Zhu, T.; Zhang, S. *ACS Nano* **2013**, *7* (4), 3427−3433.
(20) McDowell, M. T.; Lee, S. W.; Nix, W. D.; Cui, Y. *Adv. Mater.* **2013**, *25* (36), 4966−4985.
(21) Nie, A.; Gan, L.-Y.; Cheng, Y.; Asayesh-Ardakani, H.; Li, Q.; Dong, C.; Tao, R.; Mashayek, F.; Wang, H.-T.; Schwingenschlögl, U.; Klie, R. F.; Yassar, R. S. *ACS Nano* **2013**, *7* (7), 6203−6211.
(22) Liu, X. H.; Wang, J. W.; Huang, S.; Fan, F.; Huang, X.; Liu, Y.; Krylyuk, S.; Yoo, J.; Dayeh, S. A.; Davydov, A. V.; Mao, S. X.; Picraux, S. T.; Zhang, S.; Li, J.; Zhu, T.; Huang, J. Y. *Nat. Nanotechnol.* **2012**, *7* (11), 749−756.
(23) Niu, J.; Kushima, A.; Qian, X.; Qi, L.; Xiang, K.; Chiang, Y.-M.; Li, J. *Nano Lett.* **2014**, *14* (7), 4005−4010.
(24) Wang, F.; Yu, H.-C.; Chen, M.-H.; Wu, L.; Pereira, N.; Thornton, K.; Van der Ven, A.; Zhu, Y.; Amatucci, G. G.; Graetz, J. *Nat. Commun.* **2012**, *3*, 1201.
(25) Su, Q.; Dong, Z.; Zhang, J.; Du, G.; Xu, B. *Nanotechnology* **2013**, *24* (25), 255705.
(26) Luo, L.; Wu, J.; Xu, J.; Dravid, V. P. *ACS Nano* **2014**, *8* (11), 11560−11566.
(27) Zhang, H.-T.; Wu, G.; Chen, X.-H. *Langmuir* **2005**, *21* (10), 4281−4282.
(28) Evans, H. T. *Z. Kristallogr. - Cryst. Mater.* **1979**, *150* (1−4), 299−320.
(29) Buerger, M. J.; Wuensch, B. J. *Science* **1963**, *141* (3577), 276−277.
(30) Rivest, J. B.; Fong, L.-K.; Jain, P. K.; Toney, M. F.; Alivisatos, A. P. *J. Phys. Chem. Lett.* **2011**, *2* (19), 2402−2406.
(31) Takeda, H.; Donnay, J. D. H.; Roseboom, E. H.; Appleman, D. E. *Z. Kristallogr.* **1967**, *125*, 404−413.
(32) Lukashev, P.; Lambrecht, W. R. L.; Kotani, T.; van Schilfgaarde, M. *Phys. Rev. B* **2007**, *76* (19), 195202.
(33) Luther, J. M.; Jain, P. K.; Ewers, T.; Alivisatos, A. P. *Nat. Mater.* **2011**, *10* (5), 361−366.
(34) Sands, T. D.; Washburn, J.; Gronsky, R. *Phys. Status Solidi A* **1982**, *72* (2), 551−559.
(35) Lotfipour, M.; Machani, T.; Rossi, D. P.; Plass, K. E. *Chem. Mater.* **2011**, *23* (12), 3032−3038.
(36) Zhao, Y.; Pan, H.; Lou, Y.; Qiu, X.; Zhu, J.; Burda, C. *J. Am. Chem. Soc.* **2009**, *131* (12), 4253−4261.
(37) Yin, Y.; Rioux, R. M.; Erdonmez, C. K.; Hughes, S.; Somorjai, G. A.; Alivisatos, A. P. *Science* **2004**, *304* (5671), 711−714.
(38) Wang, D.-Y.; Jiang, Y.-T.; Lin, C.-C.; Li, S.-S.; Wang, Y.-T.; Chen, C.-C.; Chen, C.-W. *Adv. Mater.* **2012**, *24* (25), 3415−3420.
(39) Wang, F.; Robert, R.; Chernova, N. A.; Pereira, N.; Omenya, F.; Badway, F.; Hua, X.; Ruotolo, M.; Zhang, R.; Wu, L.; Volkov, V.; Su,

DOI: 10.1021/nl504436m
Nano Lett. XXXX, XXX, XXX−XXX

D.; Key, B.; Whittingham, M. S.; Grey, C. P.; Amatucci, G. G.; Zhu, Y.; Graetz, J. *J. Am. Chem. Soc.* **2011**, *133* (46), 18828−18836.
(40) Débart, A.; Dupont, L.; Patrice, R.; Tarascon, J. M. *Solid State Sci.* **2006**, *8* (6), 640−651.
(41) Su, Q.; Xie, J.; Zhang, J.; Zhong, Y.; Du, G.; Xu, B. *ACS Appl. Mater. Interfaces* **2014**, *6* (4), 3016−3022.
(42) Su, Q.; Du, G.; Zhang, J.; Zhong, Y.; Xu, B.; Yang, Y.; Neupane, S.; Kadel, K.; Li, W. *ACS Nano* **2013**, *7* (12), 11379−11387.
(43) Morcrette, M.; Rozier, P.; Dupont, L.; Mugnier, E.; Sannier, L.; Galy, J.; Tarascon, J. M. *Nat. Mater.* **2003**, *2* (11), 755−761.
(44) McKinnon, W. R.; Dahn, J. R. *Solid State Commun.* **1984**, *52* (3), 245−248.
(45) Jache, B.; Mogwitz, B.; Klein, F.; Adelhelm, P. *J. Power Sources* **2014**, *247* (0), 703−711.
(46) Wang, L.-W. *Phys. Rev. Lett.* **2012**, *108* (8), 085703.
(47) Pauporté, T.; Vedel, J. *Solid State Ionics* **1999**, *116* (3−4), 311−320.
(48) Cassaignon, S.; Pauporté, T.; Guillemoles, J. F.; Vedel, J. *Ionics* **1998**, *4* (5−6), 364−371.
(49) Chen, J. H.; Harvey, W. W. *Metall. Trans. B* **1975**, *6* (2), 331−339.

DOI: 10.1021/nl504436m
Nano Lett. XXXX, XXX, XXX−XXX